

## ARECIBO OBSERVATIONS OF FORMALDEHYDE IN L1551

ESTEBAN ARAYA

Physics Department, New Mexico Institute of Mining and Technology, 801 Leroy Place, Socorro, NM 87801

PETER HOFNER

Physics Department, New Mexico Institute of Mining and Technology, 801 Leroy Place, Socorro, NM 87801; and National Radio Astronomy Observatory, P.O. Box O, Socorro, NM 87801

LUCA OLMI

Physics Department, University of Puerto Rico at Rio Piedras, P.O. Box 23343, Rio Piedras, PR 00931-3300; and Istituto di Radioastronomia, INAF, Sezione di Firenze, Largo Enrico Fermi 5, I-50125 Florence, Italy

STAN KURTZ

Centro de Radioastronomía y Astrofísica, UNAM, Apartado Postal 3-72, 58089 Morelia, Michoacán, Mexico

AND

HENDRIK LINZ

Max-Planck-Institut für Astronomie, Königstuhl 17, D-69117 Heidelberg, Germany

Received 2006 April 14; accepted 2006 July 11

### ABSTRACT

We report observations of the formaldehyde ( $\text{H}_2\text{CO}$ ) 6 cm (4.8 GHz) line toward L1551. The observations were conducted with the Arecibo Telescope (beam FWHP  $\sim 1'$ ) to verify the tentative detection of  $\text{H}_2\text{CO}$  thermal emission reported by Duncan and collaborators in 1987. The  $\text{H}_2\text{CO}$  emission lines were expected to be present with a signal-to-noise ratio of  $\gtrsim 10$  in our spectra. However, we did not detect  $\text{H}_2\text{CO}$  emission; i.e., our data rule out their tentative detection. The absence of  $\text{H}_2\text{CO}$  emission is also confirmed by the fact that the  $\text{H}_2\text{CO}$  line profiles at the two positions of expected emission are well fitted by a single absorption component (accounting for the hyperfine structure of the line) in one of the positions and by a single absorption line plus a red-wing absorption component in the second position. The Orion BN/KL region remains the only  $\text{H}_2\text{CO}$  6 cm thermal emitter known. Our observations also demonstrate that the  $\text{H}_2\text{CO}$  6 cm absorption line traces not only the quiescent molecular cloud but also the kinematics associated with the star formation process in L1551–IRS 5.

*Key words:* ISM: individual (L1551) — ISM: molecules — radio lines: ISM — stars: formation

*Online material:* machine-readable table

### 1. INTRODUCTION

The 6 cm transition of formaldehyde ( $\text{H}_2\text{CO}$ ;  $J_{K_a, K_c} = 1_{11}-1_{10}$ ) has been detected toward hundreds of Galactic sources for more than 30 years (e.g., Downes et al. 1980; Watson et al. 2003; Sewilo et al. 2004). The  $\text{H}_2\text{CO}$  6 cm line is commonly observed in absorption against Galactic continuum sources (e.g., Araya et al. 2002), as well as against the 2.7 K cosmic microwave background (CMB; Palmer et al. 1969). Models including  $\text{H}_2\text{CO}$ - $\text{H}_2$  collisional excitation have been successful in explaining the low excitation temperature ( $T_{\text{ex}} \lesssim 2$  K) of the  $\text{H}_2\text{CO}$  6 cm transition required for absorption against the CMB (Garrison et al. 1975). These models predict that the cooling mechanism operates at densities lower than  $10^5 \text{ cm}^{-3}$ . At densities above  $\sim 10^5 \text{ cm}^{-3}$  the molecules are “thermalized,” and the  $\text{H}_2\text{CO}$  6 cm transition turns into emission.

$\text{H}_2\text{CO}$  6 cm emission is an uncommon phenomenon; it has only been confirmed toward three extragalactic regions as megamaser emission (Araya et al. 2004a) and five Galactic regions as maser emission (Araya et al. 2005, 2006 and references therein), and only the Orion BN/KL region has been confirmed as a thermal  $\text{H}_2\text{CO}$  6 cm emitter (Zuckerman et al. 1975).

Duncan et al. (1987) reported the tentative detection of two  $\text{H}_2\text{CO}$  6 cm thermal emission regions in L1551. They used the Very Large Array D configuration for their observations, and due to the presence of extended absorption and sparse  $u$ - $v$  sampling, they were not able to ascertain whether the emission features

were real or interferometric artifacts. According to their Figure 4, the two tentative emission regions are  $\lesssim 1'$  in size and are located approximately  $4'$  apart. In this work we report Arecibo observations (beam FWHP  $\sim 1'$ ) intended to further investigate the presence of  $\text{H}_2\text{CO}$  6 cm thermal emission in the L1551 region.

#### 1.1. The L1551–IRS 5 Star-Forming Region

L1551 is a region of low-mass star formation located at a distance of  $\sim 140$  pc (Kenyon et al. 1994) within the Taurus-Auriga molecular cloud. The L1551 region shows a bipolar molecular outflow whose origin coincides with the infrared source IRS 5 (e.g., Goodman et al. 1993). The outflow has a southwest-northeast orientation from blueshifted to redshifted gas and shows a peculiar hollow cylindrical morphology (Uchida et al. 1987). Based on their CO observations, Uchida et al. (1987) found that the walls of the hollow cylinders have a velocity gradient perpendicular to the direction of the outflow that would indicate rotation of the molecular gas in the outflow.  $\text{H}_2\text{CO}$  6 cm observations of the region conducted by Sandqvist & Bernes (1980) with the 100 m Effelsberg telescope (beamwidth  $\sim 2.6'$ ) show that L1551–IRS 5 is located at the southeastern edge of a molecular cloud core. At much higher angular resolution, Rodríguez et al. (2003) found that the IRS 5 region harbors two collimated jets of ionized gas that have the same position angle as the CO outflow. The morphology of the jets is consistent with the presence of a binary system in L1551–IRS 5 (see also Rodríguez et al. 1998). Recently, Takakuwa

et al. (2004) reported  $\sim 3''$  resolution observations of CS  $J = 7-6$  toward L1551-IRS 5. Their observations reveal a disklike structure perpendicular to the axis of the radio jets and with a clear southeast (blueshifted)–northwest (redshifted) velocity gradient that is consistent with rotation.

## 2. OBSERVATIONS

The observations were conducted from 2004 December 13 to 19 with the 305 m Arecibo Radio Telescope.<sup>1</sup> We observed the  $J_{K_a K_c} = 1_{10-1_{11}}$   $K$ -doublet transition of formaldehyde ( $\nu_o = 4829.6594$  MHz, i.e., the weighted average frequency of the  $F = 2-2$  and  $F = 0-1$  hyperfine components given in Tucker et al. 1970) toward 64 positions in L1551, resulting in an  $8' \times 8'$  full-beam-sampled map. The reference position of the map was R.A. =  $04^h 31^m 21^s.8$ , decl. =  $+18^\circ 05' 54''$  (J2000.0). Two independent subcorrelators were used to simultaneously observe two linear polarizations. Each subcorrelator was configured to a bandwidth of 6.25 MHz ( $\sim 400$  km s<sup>-1</sup>) and 2048 channels that resulted in an initial channel width of 3.1 kHz ( $0.19$  km s<sup>-1</sup>). The observational procedure was position switching, with a 5 minute on-source–5 minute off-source cycle. In order to minimize the effects of standing waves, the off (or reference) position was chosen such that the same elevation–azimuth path followed during the on-source observations was observed during the off-source observations.

The calibration to antenna temperature was achieved by observing a calibration signal during 10 s at the end of every on-off cycle. The system temperature derived from measurements of the calibration signal was  $\sim 32$  K. Since the gain of the telescope is a function of elevation and azimuth (e.g., Araya et al. 2004a), we chose as flux calibrator the quasar B0518+165, which has a declination similar to the L1551 region; thus, during the B0518+165 observations, the telescope followed approximately the same elevation–azimuth path as that followed during the L1551 observations. In Figure 1 we show the gain of the telescope as a function of elevation based on our B0518+165 observations. A clear elevation dependence is observed. We fitted the telescope gain with a quadratic function and applied it to every L1551 scan before averaging. In Figure 1 (*bottom*) we show the residuals of the B0518+165 gain fit. The dispersion of the residuals is smaller than 10% of the average value of the telescope gain, thus the flux calibration (with respect to B0518+165) is better than 10%. We estimate that the absolute flux calibration is better than 30%, based on our previous observations with the Arecibo Telescope (e.g., Araya et al. 2003, 2004b).

From our B0518+165 observations we also measured the telescope beamwidth, pointing accuracy, and beam efficiency ( $\eta_B$ ): the beamwidth was  $\sim 0'.87 \times 1'.04$ , the pointing accuracy was better than  $10''$ , and the averaged beam efficiency was  $\eta_B = 0.64$ . After checking the individual scans and applying the elevation-dependent telescope gain, we averaged the scans at each position and the spectra from the two orthogonal polarizations. We subtracted a linear baseline and smoothed the spectra to a final channel width of  $0.38$  km s<sup>-1</sup> (6.1 kHz). All calibration and data reduction was done using the CLASS program.<sup>2</sup>

## 3. RESULTS

### 3.1. Absence of H<sub>2</sub>CO 6 cm Emission

In Figure 2 we show the H<sub>2</sub>CO map of the L1551-IRS 5 region obtained with the Arecibo Telescope. We detected H<sub>2</sub>CO

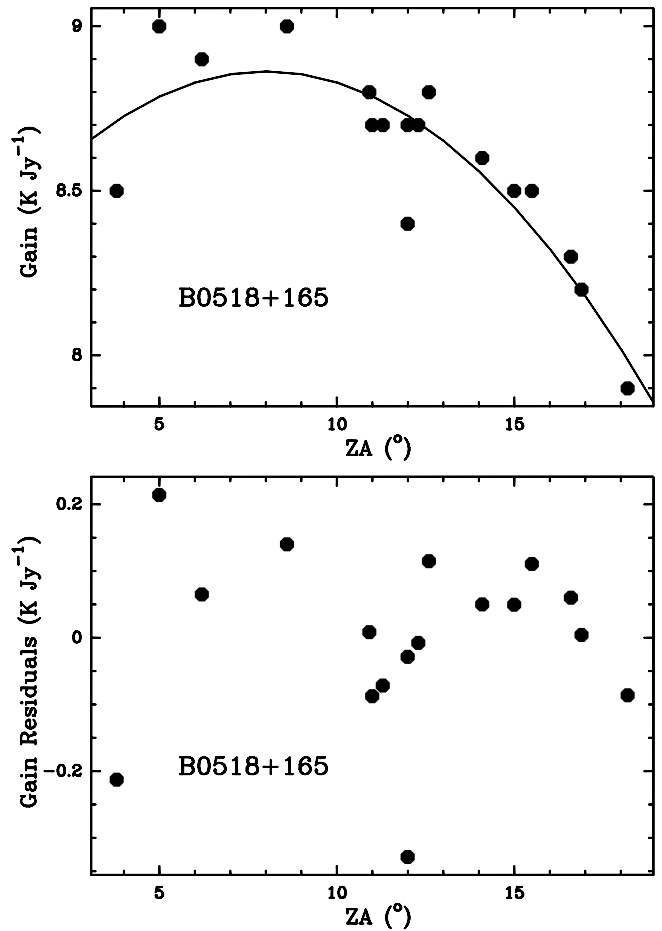


FIG. 1.—*Top*: Gain of the Arecibo Telescope as a function of zenith angle obtained by observations of the quasar B0518+165. A quadratic fit to the data is shown with a solid line. *Bottom*: Residuals of the quadratic fit of the gain measurements. The dispersion is less than 10% of the average value of the telescope gain.

absorption at every observed position, with flux densities that range between approximately  $-20$  and  $-90$  mJy. The rms of the spectra is between 1.57 and 2.85 mJy. Lower rms (i.e., greater integration time) spectra were obtained toward the positions where H<sub>2</sub>CO 6 cm thermal emission was tentatively detected by Duncan et al. (1987).

We did not detect positive H<sub>2</sub>CO features (i.e., emission lines) toward any position in the map (Fig. 2). In particular, we did not detect emission features toward the positions where Duncan et al. (1987) reported thermal H<sub>2</sub>CO emission, i.e., at offsets  $(+3', +2')$  and  $(0', 0')$ . Since H<sub>2</sub>CO emission could be masked by absorption (e.g., Kutner & Thaddeus 1971), we compared the H<sub>2</sub>CO absorption profiles surrounding the positions where H<sub>2</sub>CO emission was expected. According to Duncan et al. (1987), the H<sub>2</sub>CO emission features are contained within  $\sim 1'$  (i.e., approximately the Arecibo beam at 6 cm); thus, the H<sub>2</sub>CO 6 cm absorption profiles at the  $(+3', +2')$  and  $(0', 0')$  positions should show evidence for H<sub>2</sub>CO emission in comparison with nearby pointing positions. However, we do not find any evidence for H<sub>2</sub>CO emission blended with absorption. The H<sub>2</sub>CO absorption profiles at the positions of tentative emission differ by less than  $5\sigma$  (at the expected H<sub>2</sub>CO emission velocity) in comparison with most spectra from adjacent positions, whereas a difference greater than  $10\sigma$  was expected if the emission features reported by Duncan et al. (1987) were real. We conclude that the tentative detections of thermal H<sub>2</sub>CO 6 cm emission by Duncan et al. (1987) were artifacts.

<sup>1</sup> The Arecibo Observatory is part of the National Astronomy and Ionosphere Center (NAIC), which is operated by Cornell University under a cooperative agreement with the National Science Foundation.

<sup>2</sup> CLASS is part of the GILDAS software package developed by IRAM.

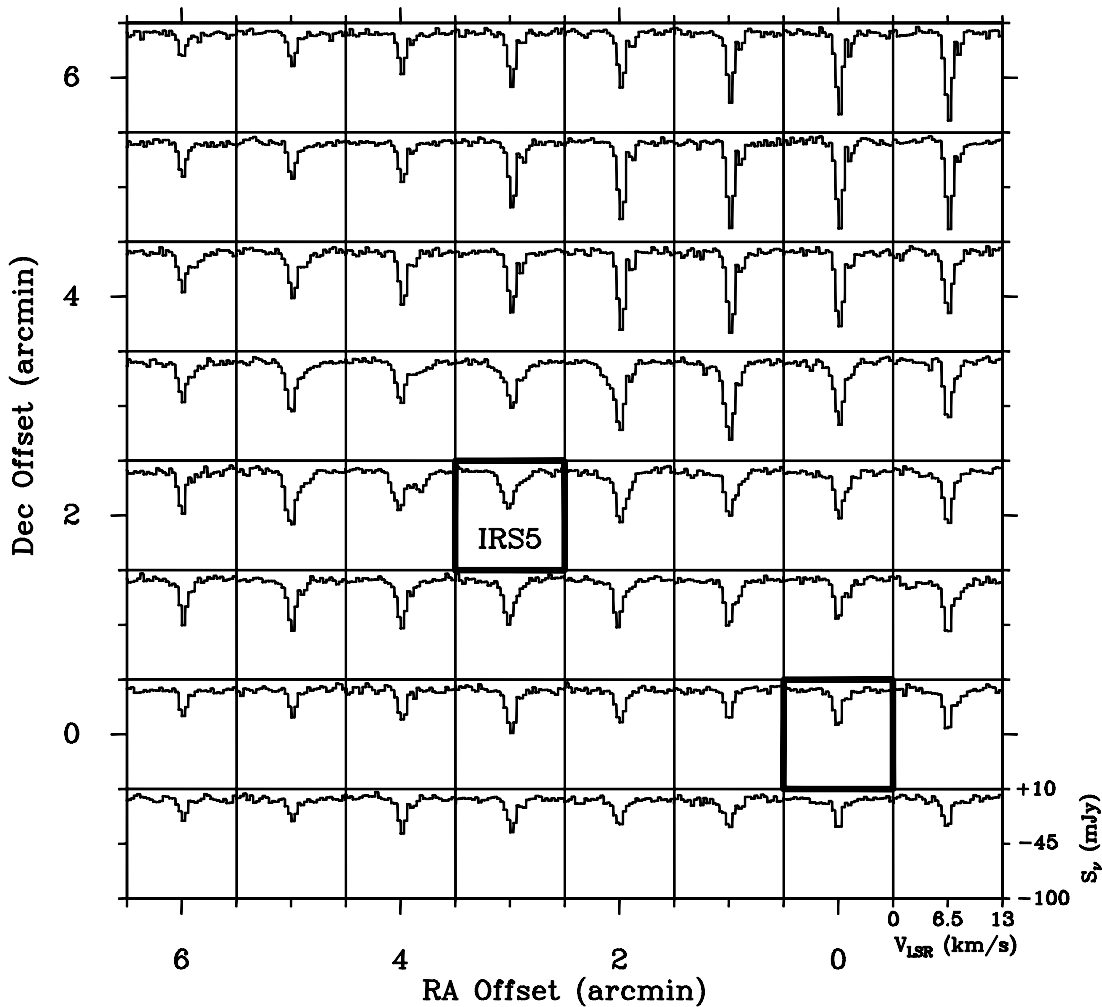


FIG. 2.—H<sub>2</sub>CO 6 cm spectra obtained toward 64 pointing positions. The location of L1551–IRS 5 corresponds approximately to the offset (+3', +2'). The observations were obtained with full-beam spacing. The locations where H<sub>2</sub>CO 6 cm thermal emission was tentatively detected by Duncan et al. (1987) are (+3', +2') and (0', 0') and are highlighted with thick squares. The reference position of the map is R.A. = 04<sup>h</sup>31<sup>m</sup>21<sup>s</sup>.8, decl. = +18°05'54'' (J2000.0).

### 3.2. Extended H<sub>2</sub>CO 6 cm Absorption in the L1551–IRS 5 Region

Turning our attention to the extended absorption (Fig. 2), the lines are stronger and narrower (full width at zero intensity  $\sim 3 \text{ km s}^{-1}$ ) toward the northwestern part of the map and broader toward the center of the map. Because the separation of the  $F = 2-2$  and  $F = 1-0$  hyperfine components of the H<sub>2</sub>CO  $K$ -doublet is  $\sim 1.13 \text{ km s}^{-1}$  (see Tucker et al. 1970), the hyperfine structure of the line significantly contributes to the line profile of most spectra. In Figure 3 we show the spectrum obtained toward the offset position (+3', +3'). Dashed lines mark the positions and relative strengths of the hyperfine components of the H<sub>2</sub>CO 6 cm transition. The spectrum shown in Figure 3 has a (red) asymmetry that is clearly due to the  $F = 1-0$  hyperfine component. The spectrum also shows contribution to the line profile from redshifted and blue-shifted gas. In order to check whether such redshifted and blue-shifted wings trace organized motion of the molecular gas in the region, we obtained a velocity-integrated map of the redshifted, line-core, and blueshifted gas. To construct the map, we integrated velocity ranges corresponding to the spacing of four channels at the red, core, and blue velocities, as shown in Figure 3. The blue and red ranges were chosen such that they are separated by approximately 1.5 channels from the frequency of the nearest hyperfine component. This was done to reduce contamination from the

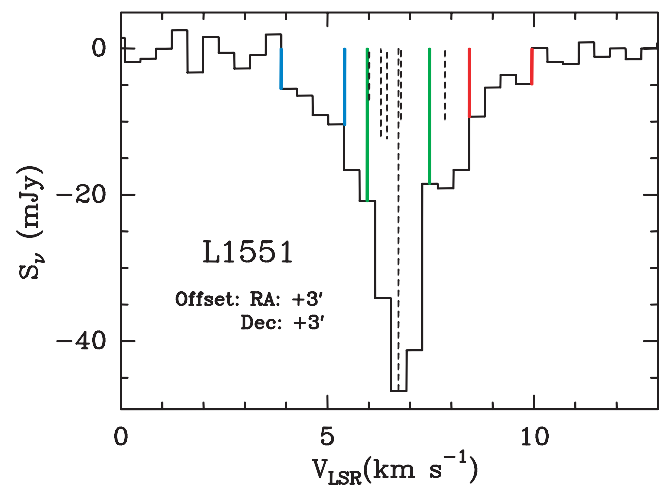


FIG. 3.—H<sub>2</sub>CO 6 cm spectrum obtained toward the (+3', +3') position. The dashed lines show the relative velocity and strength of the six hyperfine components of the H<sub>2</sub>CO 6 cm transition. Note the (red) asymmetry caused by the  $F = 1-0$  component and the red and blue wings. With blue, green, and red lines we show the velocity ranges that were used to obtain the map shown in Fig. 4.

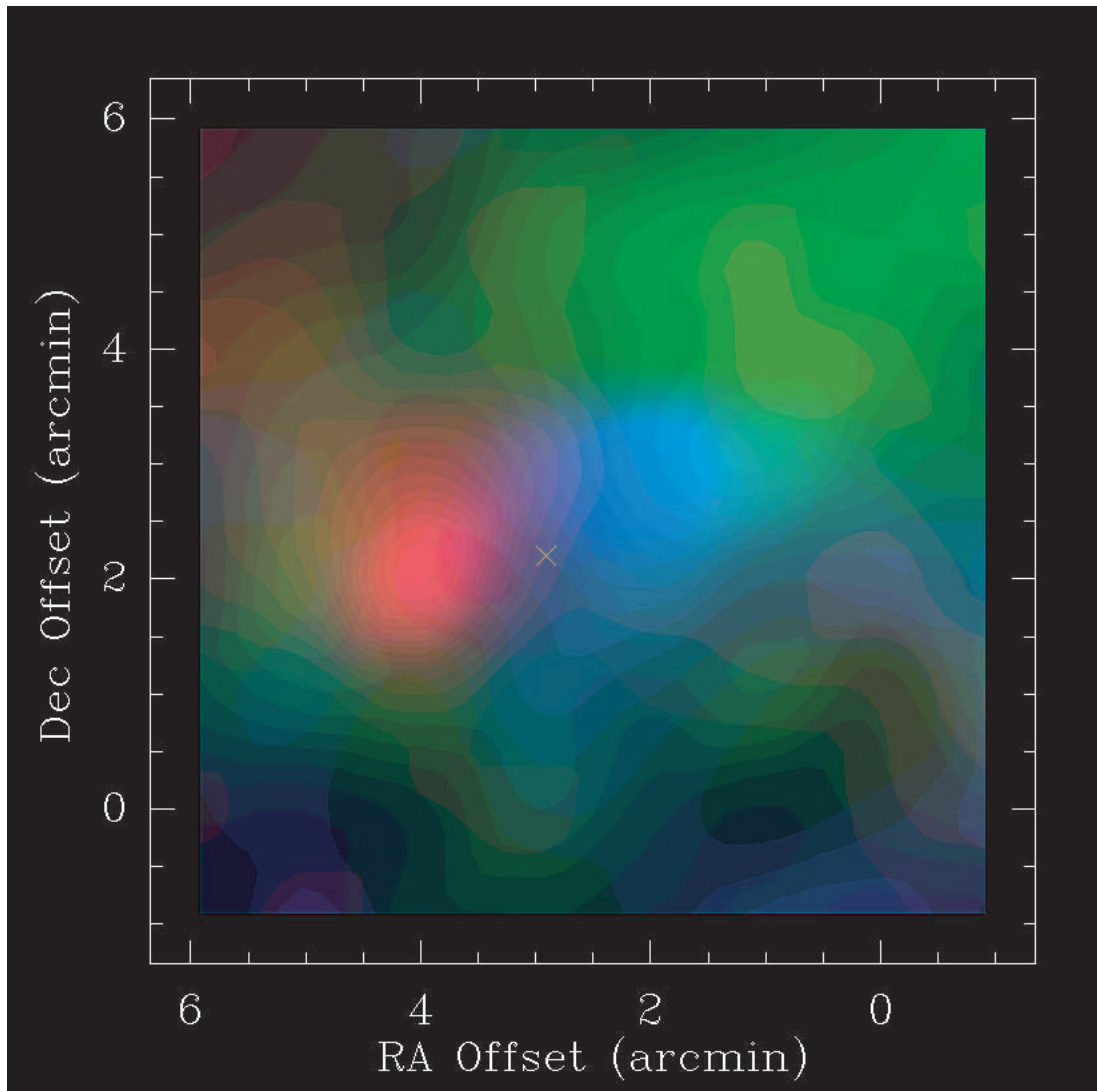


FIG. 4.—Integrated-intensity map of the  $\text{H}_2\text{CO}$  absorption. The red, green, and blue contours were obtained by integrating the flux density within the velocity ranges shown in Fig. 3. The line-core portion of the map (*green*) was arbitrarily saturated, and its brightness was decreased to highlight the brightness distribution of the redshifted and blueshifted gas. We detected absorption at every position in the map; the absence of green in the map implies *weaker* absorption, not absence of absorption. The position of L1551-IRS 5 is marked with a yellow cross. The reference position of the map is R.A. =  $04^{\text{h}}31^{\text{m}}21^{\text{s}}.8$ , decl. =  $+18^{\circ}05'54''$  (J2000.0). Note the presence of two velocity gradients: one clearly oriented in an approximately southeast-northwest direction and contained within  $\sim 2'$  from the position of L1551-IRS 5 and a weaker and less collimated velocity gradient oriented in a northeast-southwest direction at distances larger than  $2'$  from L1551-IRS 5.

hyperfine structure to the kinematics traced by the wings of the  $\text{H}_2\text{CO}$  spectra. In Figure 4 we show a map of the integrated intensity of the red, green, and blue velocity ranges, as shown in Figure 3.

The distribution of the line-core absorption (Fig. 4, *green contours*) has two main features: the absorption is more intense toward the northwestern part of the map, and there is a ringlike distribution of strong (more green)  $\text{H}_2\text{CO}$  absorption centered approximately  $1'$  east of L1551-IRS 5. A different representation of the ringlike structure to the east of IRS 5 is given in Figure 5, where we show (*black line*) the averaged spectrum of the four positions inside the ring [(+3', +2'), (+4', +2'), (+3', +3'), and (+4', +3')]. We also show (*green line*) the average of nine pointing positions along the ring and the difference (*red line*) between the inner ring average spectrum (*black line*) and the ring average spectrum (*green line*). Note the apparent  $\sim 8$  mJy emission peak (red spectrum) at the velocity of the  $\text{H}_2\text{CO}$  line core, due to weaker absorption in the inner ring region (Fig. 5).

The weak absorption in the inner region of the ring could be caused by (1) extended  $\text{H}_2\text{CO}$  emission blended with absorption,

(2) different excitation conditions in the inner ring region and/or depletion, or (3)  $\text{H}_2\text{CO}$  gas that has been redistributed in velocity by the outflow. If possibility 1 were correct, then the  $\text{H}_2\text{CO}$  emission would be more extended and substantially weaker than that tentatively detected by Duncan et al. (1987); i.e., the apparent emission cannot correspond to the emission reported by Duncan et al. (1987). Option 2 is clearly possible given that L1551-IRS 5 is located just  $\sim 1'$  west of the center of the ring. However, the third possibility could be the main cause of the weak absorption in the inner ring, because the red spectrum in Figure 5 shows, in addition to the apparent emission, two absorption components at high and low velocities. This is consistent with the interpretation that some molecular gas has been redistributed in velocity from the line core into the line wings by the outflow in the region. An equivalent way of expressing this idea is that the total area under the red spectrum in Figure 5 is approximately zero; hence, in the case of optically thin conditions, the difference between the black and green spectra (Fig. 5) would imply a redistribution of the gas in velocity space.

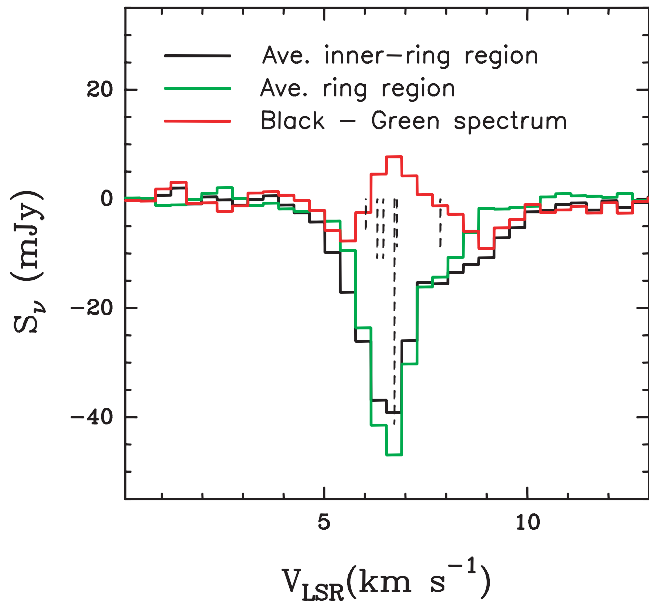


FIG. 5.—Representation of the weak H<sub>2</sub>CO absorption region (inner ring region) to the east of IRS 5 (see Fig. 4, *green contours*), which is surrounded by a ring of strong H<sub>2</sub>CO absorption. *Black line*: Average of the (+3', +2'), (+4', +2'), (+3', +3'), and (+4', +3') spectra (i.e., inner ring spectra). *Green line*: Average of 9 of the 12 spectra that surround the four pointing positions used to obtain the black spectrum (i.e., H<sub>2</sub>CO ring). The three pointing positions excluded are (+3', +4'), (+2', +4'), and (+2', +3') because they are part of the strong absorption toward the northwestern part of the map. *Red line*: Difference between the green and black spectra. We show the hyperfine components of the H<sub>2</sub>CO 6 cm line (*dashed lines*).

### 3.3. H<sub>2</sub>CO Velocity Gradients in the L1551–IRS 5 Region

The most significant feature of Figure 4 is the bipolar distribution of redshifted and blueshifted H<sub>2</sub>CO, centered approximately at the position of L1551–IRS 5 and oriented in an approximately southeast-northwest direction (hereafter referred to as the “southeast-northwest velocity gradient”). The presence of blue and red wings in the spectra around the position of IRS 5 is clear from inspection of Figure 2. Although possible in other positions, in only one case, offset (+4', +2'), does the H<sub>2</sub>CO spectrum seem to be a superposition of two H<sub>2</sub>CO clumps (note that the separation of the two components is  $\sim 2.4$  km s<sup>-1</sup>; thus, it cannot be due to the hyperfine structure of the H<sub>2</sub>CO 6 cm line). However, pointing positions adjacent to (+4', +2') clearly show red wings; thus, the redshifted clump to the east of IRS 5 likely traces gas kinematics.

A second and weaker velocity gradient from the line wings is also observed in Figure 4. The red contours extend primarily toward the northeastern part of the map, and the blue contours tend to extend toward the southwestern part of the map (hereafter referred to as the “northeast-southwest velocity gradient”). As mentioned in § 1.1, the CO outflow in the region extends northeast-southwest from redshifted to blueshifted material, respectively (e.g., Goodman et al. 1993), which is also collinear with the binary jet in the region (Rodríguez et al. 2003). Thus, the northeast-southwest velocity gradient detected in H<sub>2</sub>CO is likely to be a consequence of the L1551–IRS 5 outflow.

The nature of the southeast-northwest velocity gradient is more difficult to ascertain. At first glance, the southeast-northwest velocity gradient is almost perpendicular to the direction of the CO outflow, which might indicate that this H<sub>2</sub>CO velocity gradient is tracing a molecular torus around IRS 5. However, this is unlikely, because higher angular resolution observations of the region by Takakuwa et al. (2004) show a CS  $J = 7-6$  velocity

gradient oriented approximately northwest (redshifted)–southeast (blueshifted) that is likely due to rotation, which is opposite to the velocity gradient of the southeast-northwest H<sub>2</sub>CO component (Fig. 4). CO observations offer a better clue to the nature of the southeast-northwest H<sub>2</sub>CO velocity gradient: a comparison of the position and velocity of the southeast-northwest H<sub>2</sub>CO gradient with respect to CO maps of the region (Moriarty-Schieven et al. 1987; Uchida et al. 1987) suggests that the bipolar structure is tracing the molecular outflow or, more specifically, the inner regions of the molecular outflow. The CO velocity maps in Moriarty-Schieven et al. (1987) and Uchida et al. (1987) show that, within  $\sim 2'$  from the position of L1551–IRS 5, the CO velocity gradient is mainly oriented in an approximately southeast-northwest direction, which agrees with the orientation of the southeast-northwest H<sub>2</sub>CO velocity gradient.

## 4. ANALYSIS AND DISCUSSION

### 4.1. A Model of the H<sub>2</sub>CO Line Profiles

The H<sub>2</sub>CO 6 cm line shapes can be modeled assuming that, for a given line of sight, the medium has a constant opacity, a single velocity component, and a fixed excitation temperature. These assumptions are clearly an oversimplification of the problem; however, they allow us to obtain a simple solution of the radiative transfer equation (in the form of the expected flux density), i.e.,

$$S_{\nu}^{\text{expected}}(T_{\text{ex}}, \tau_{\nu}) = \frac{2h\Omega\nu_o^3}{\gamma c^2} \left( \frac{1}{e^{h\nu_o/k_B T_{\text{ex}}} - 1} - \frac{1}{e^{h\nu_o/k_B T_{\text{CMB}}} - 1} \right) \times (1 - e^{-\tau_{\nu}(v)}), \quad (1)$$

where  $S_{\nu}^{\text{expected}}$  is the flux density spectrum expected from on-off observations with the Arecibo Telescope using a pointlike gain calibration;  $\Omega$  is the effective solid angle of the Arecibo beam (i.e.,  $\Omega = 1.133\theta_{\text{min}}\theta_{\text{max}}$ , assuming a Gaussian power pattern);  $T_{\text{CMB}}$  is 2.7 K, the temperature of the CMB radiation against which H<sub>2</sub>CO absorption occurs; and the factor  $\gamma$  corrects for the systematic calibration effect of applying a point-source gain curve, in spite of the fact that the H<sub>2</sub>CO absorption is extended (Fig. 2). We estimate the numerical value of  $\gamma$  to be 0.827.<sup>3</sup>

The H<sub>2</sub>CO 6 cm  $K$ -doublet is composed of six hyperfine transitions (Tucker et al. 1970). In order to model the six hyperfine lines, the optical depth can be written as (e.g., Heiles 1973)

$$\tau_{\nu}(v) = \tau \sum_{i=1}^6 r_i e^{-(v - V_{\text{LSR}} - \Delta v_i)^2 / \Delta V^2}, \quad (2)$$

where  $V_{\text{LSR}}$  is the LSR velocity of the  $F = 2-2$  component,  $\Delta v_i$  are the velocity differences of the hyperfine lines with respect to the  $F = 2-2$  transition,  $\Delta V$  is the line width<sup>4</sup> of the hyperfine lines measured in kilometers per second (assumed equal for all of them),  $\tau$  is the optical depth of the  $F = 2-2$  component,  $r_i$  are the line strength ratios with respect to the  $F = 2-2$  line, and the velocity  $v$  is the independent variable.

We used equations (1) and (2) to model the observed line profiles at each pointing position. The free parameters of the model are the velocity of the  $F = 2-2$  hyperfine component ( $V_{\text{LSR}}$ ), the line width ( $\Delta V$ ) of the hyperfine lines, the optical depth ( $\tau$ ), and the excitation temperature ( $T_{\text{ex}}$ ). We used a minimum  $\chi^2$  method (e.g.,

<sup>3</sup> The factor  $\gamma$  is defined as  $\gamma = S_{\nu}^{\text{extended}}/S_{\nu}^{\text{point}}$ , where  $S_{\nu}^{\text{extended}}$  (Jy) =  $2.946 \times 10^{-3} \theta_{\text{min}} \theta_{\text{max}} \nu$  (GHz)<sup>2</sup>  $T_A$  (K)/ $\eta_B$  and  $S_{\nu}^{\text{point}}$  (Jy) =  $T_A$  (K)/gain (K Jy<sup>-1</sup>).

<sup>4</sup> The FWHM of the line is equal to  $[4 \ln(2)]^{1/2} \Delta V$  in the case of an optically thin line.

TABLE 1  
MODEL RESULTS

Offset (arcmin, arcmin)	$T_{\text{ex}}$ (K)	Optical Depth	$\Delta V$ (km s <sup>-1</sup> )	$V_{\text{LSR}}$ (km s <sup>-1</sup> )	$\chi^2$ <sup>a,b</sup>
(-1, -1) .....	[1.18, 2.10]	[0.17, 0.53]	[0.42, 0.47]	[6.53, 6.60]	4.72
(0, -1) .....	[1.10, 2.23]	[0.20, 0.90]	[0.34, 0.40]	[6.61, 6.68]	13.3 (4.72)
(+1, -1) .....	[1.63, 2.42]	[0.30, 2.23]	[0.39, 0.65]	[6.49, 6.80]	23.5
(+2, -1) .....	[1.29, 2.40]	[0.16, 1.34]	[0.47, 0.57]	[6.56, 6.69]	7.78 (4.72)
(+3, -1) .....	[1.99, 2.26]	[0.60, 1.35]	[0.36, 0.43]	[6.83, 6.91]	7.78

NOTE.—Table 1 is published in its entirety in the electronic edition of the *Astronomical Journal*. A portion is shown here for guidance regarding its form and content.

<sup>a</sup> In some cases the  $\Delta V$  and  $V_{\text{LSR}}$  parameters converge within a given  $\chi^2$  value, whereas the  $\tau$  and  $T_{\text{ex}}$  parameters show multiple solutions for the same  $\chi^2$  contour level. For those cases we report  $\Delta V$  and  $V_{\text{LSR}}$  ranges for a different  $\chi^2$  contour level (shown in parentheses) than that used to obtain the  $\tau$  and  $T_{\text{ex}}$  ranges.

<sup>b</sup> When  $\chi^2$  values of less than 23.5 were obtained, we explored the convergence of the parameters at fixed  $\chi^2$  levels, i.e.,  $\chi^2 = 4.72, 7.78, 9.70, 13.3, 16.3,$  and  $23.5$ , which correspond to confidence levels of 68.3%, 90.0%, 95.4%, 99.0%, 99.73%, and 99.99% for a 4 degrees of freedom  $\chi^2$  fitting (Press et al. 1999). When convergence better than the  $\chi^2 = 23.5$  value was not achieved, arbitrary  $\chi^2$  levels were used.

Press et al. 1999) to determine the region in the  $\{V_{\text{LSR}}, \Delta V, \tau, T_{\text{ex}}\}$  space for the best fit of the line profiles. In Table 1 we report the results of the model for each of the 64 pointing positions. We give the ranges of the free parameters within the listed  $\chi^2$  values (lower  $\chi^2$  values imply a better convergence of the model). We found that the  $\Delta V$  and  $V_{\text{LSR}}$  parameters showed better convergence than the  $T_{\text{ex}}$  and the optical depth.

In Figure 6 we show the results of the model for three pointing positions. The observed spectra are shown with a thick line, and the best fit is shown with a thin line. We also include the  $\chi^2$  maps for  $\Delta V$  versus  $V_{\text{LSR}}$  and  $\tau$  versus  $T_{\text{ex}}$ . The top row shows an example of a good fit, where convergence better than  $\chi^2 = 4.72$  (i.e., 68.3% confidence level; Press et al. 1999) was achieved. Note in addition that this spectrum corresponds to the offset ( $0', 0'$ ), i.e., one of the positions where Duncan et al. (1987) reported tentative H<sub>2</sub>CO emission. The good fit of the line profile by a single-velocity H<sub>2</sub>CO absorption component also confirms the absence of H<sub>2</sub>CO emission at the ( $0', 0'$ ) position.

An example of a less good fit is shown in Figure 6 (*middle row*), where a convergence just better than  $\chi^2 = 13.3$  (99.0% confidence level; Press et al. 1999) was obtained. Finally, in the bottom row of Figure 6 we show an example of a spectrum that could not be successfully fitted due to the presence of blueshifted gas. Figure 6 exemplifies that  $\Delta V$  and  $V_{\text{LSR}}$  show better convergence properties than  $\tau$  and  $T_{\text{ex}}$ : note that the  $\chi^2$  curves are concentric ellipses in the case of the  $\{\Delta V, V_{\text{LSR}}\}$  space, whereas in the case of the  $\{\tau, T_{\text{ex}}\}$  space ellipses are obtained only when a good fit is achieved. The  $\tau$  versus  $T_{\text{ex}}$  confidence-level plots also show an inherent degeneracy between these free parameters: a good fit could be achieved by a higher optical depth and higher excitation temperature or by a lower optical depth and lower excitation temperature. We conclude that our model determines the  $\Delta V$  and  $V_{\text{LSR}}$  values (of the line core) reasonably well, whereas it can only give a rough estimate of the  $\tau$  and  $T_{\text{ex}}$  values. We found that the  $T_{\text{ex}}$  value of the H<sub>2</sub>CO 6 cm lines is smaller than  $\sim 2.5$  K for all pointing positions, and the optical depth ranges between  $\sim 0.1$  and 2.9. Due to the large range in the possible  $\tau$  and  $T_{\text{ex}}$  values (i.e., poor convergence), an analysis of the spatial distribution of these parameters is not feasible, nor is it possible to estimate the H<sub>2</sub>CO column density in the region.<sup>5</sup> Nevertheless, the excitation tem-

perature ranges are consistent with those reported by Sandqvist & Bernes (1980) based on multitransition (but lower angular resolution at 6 cm) H<sub>2</sub>CO observations. The  $\tau$  and  $T_{\text{ex}}$  values we obtained are also comparable to H<sub>2</sub>CO values derived for other low-mass molecular cloud cores (e.g., Young et al. 2004). In the case of the  $\Delta V$  and  $V_{\text{LSR}}$  values, a study of their spatial distribution is possible given the better convergence of these parameters (see below).

#### 4.2. H<sub>2</sub>CO 6 cm Absorption: A Tracer of the Molecular Gas Kinematics in the L1551–IRS 5 Region

As mentioned in § 4.1, the  $\Delta V$  and  $V_{\text{LSR}}$  parameters successfully converged in our fitting procedure, thus a study of the spatial distribution of these parameters is possible.<sup>6</sup> To do this, we assumed as a best-fit value of  $\Delta V$  and  $V_{\text{LSR}}$  the middle point of their ranges given in Table 1, which closely corresponds to the geometric center of the confidence-level ellipses (see Fig. 6, *middle column*). We found that the  $V_{\text{LSR}}$  (i.e., the velocity of the H<sub>2</sub>CO line core) just southeast of IRS 5 is preferentially blueshifted with respect to other places in the map and shows a northeast-southwest elongation. However, a lower rms noise and more extended (ideally half-beam-sampled) map is required to verify whether the H<sub>2</sub>CO 6 cm line core velocity is tracing the molecular outflow in L1551.

In Figure 7 we show the distribution of the line width ( $\Delta V$ ). The maximum line width is coincident with the location of L1551–IRS 5. This implies that the H<sub>2</sub>CO 6 cm line is tracing the kinematics of the molecular gas close to L1551–IRS 5, where the width of the H<sub>2</sub>CO absorption lines can be significantly modified by the molecular outflow and possibly by the rotation of a molecular torus. The  $\Delta V$  distribution also shows an “hourglass” morphology in the direction of the CO outflow (clearly apparent toward the southwestern part of the map but also possibly toward the east-northeast of L1551–IRS 5), which demonstrates that H<sub>2</sub>CO is indeed tracing the molecular outflow in L1551–IRS 5. The hourglass morphology, in particular the low velocity dispersion toward the southwest in Figure 7, resembles the CO morphology observed by Uchida et al. (1987; see also Moriarty-Schieven et al. 1987).

These results, together with the velocity gradients traced by the line wings as shown in Figure 4, demonstrate that H<sub>2</sub>CO 6 cm

<sup>5</sup> The H<sub>2</sub>CO molecules are not in thermal equilibrium (e.g., the 6 cm K-doublet excitation temperature is lower than the CMB temperature); thus, a detailed excitation analysis (which must include other H<sub>2</sub>CO transitions) is required to reliably determine the H<sub>2</sub>CO column density.

<sup>6</sup> A direct analysis of the  $\Delta V$  and  $V_{\text{LSR}}$  parameters from the observed spectra (i.e., without the fitting procedure discussed in § 4.1) is not adequate because the hyperfine structure of the absorption profiles must be taken into account.

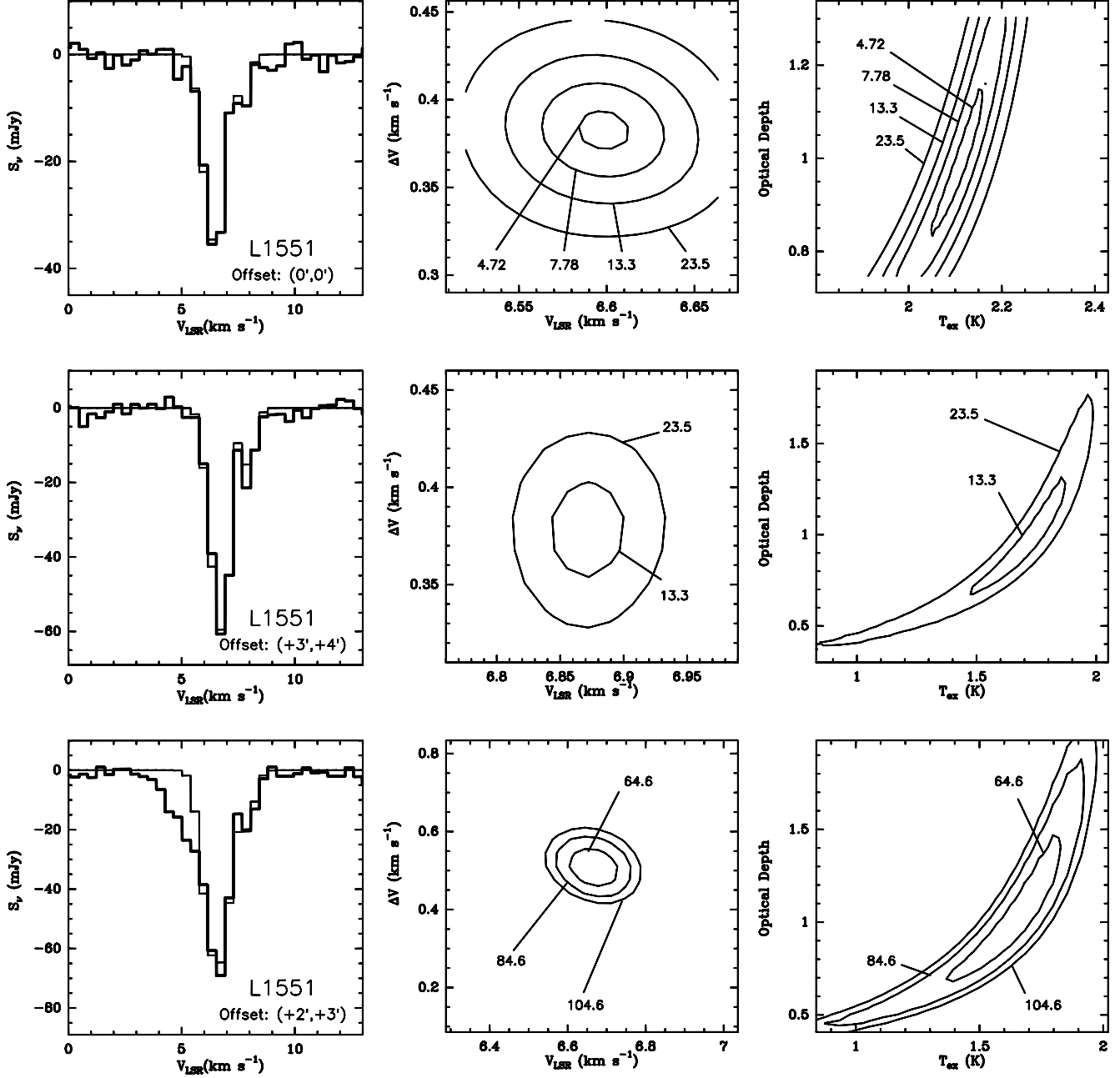


FIG. 6.—Examples of the modeling of the  $\text{H}_2\text{CO}$  absorption profiles. The three rows show the results for different pointing positions. The observed spectra are shown with a thick line, and the best fit is shown with a thin line. The  $\chi^2$  maps are shown for  $\Delta V$  vs.  $V_{\text{LSR}}$  and optical depth vs.  $T_{\text{ex}}$ . *Top panels:* Example of a good fit in which convergence better than  $\chi^2 = 4.72$  was achieved. *Middle panels:* Example of a less good fit. The convergence of the  $\Delta V$  and  $V_{\text{LSR}}$  parameters is better (i.e., the confidence level curves are concentric ellipses) than that of the optical depth and  $T_{\text{ex}}$ . *Bottom panels:* Bad fit of the line profile due to the presence of blueshifted material. Nevertheless, note that the line core was reasonably well fitted.

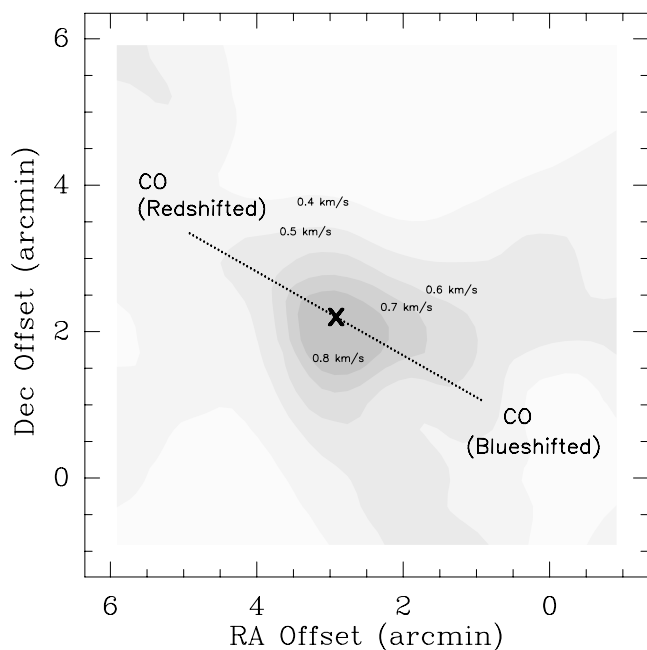


FIG. 7.—Map of the  $\Delta V$  distribution of the  $\text{H}_2\text{CO}$  absorption lines obtained by fitting the  $\text{H}_2\text{CO}$  spectra as discussed in § 4.1. The position of L1551-IRS 5 and the direction of the CO outflow are shown. The reference position of the map is R.A. =  $04^{\text{h}}31^{\text{m}}21^{\text{s}}.8$ , decl. =  $+18^{\circ}05'54''$  (J2000.0).

absorption not only traces the quiescent molecular core and its envelope (e.g., Fig. 4, *green contours*) but also carries information about the gas kinematics of the active star formation region.

## 5. SUMMARY

We report observations conducted with the Arecibo Telescope to confirm the tentative detection of  $\text{H}_2\text{CO}$  6 cm thermal emission

in L1551 (Duncan et al. 1987). Our observations conclusively show that there is no  $\text{H}_2\text{CO}$  emission at the velocity and intensity reported by Duncan et al. (1987). Thus, the Orion BN/KL region is still the only  $\text{H}_2\text{CO}$  6 cm thermal emitter known.

We also explore the properties of the extended  $\text{H}_2\text{CO}$  6 cm absorption in the region. Our observations of the  $\text{H}_2\text{CO}$  flux density distribution agree with previous lower angular resolution observations by Sandqvist & Bernes (1980) and show that, at arcminute angular resolution, the low-mass young stellar system L1551-IRS 5 is located toward the southeastern part of a molecular clump. We also detect blue and red line wings that trace two main velocity gradients: one oriented northeast-southwest that traces the molecular outflow in the region and one oriented approximately southeast-northwest and approximately centered at the position of IRS 5. This structure is likely part of the molecular outflow as well.

We find that the  $\text{H}_2\text{CO}$  line width distribution peaks at the position of L1551-IRS 5 and exhibits a morphology consistent with the hollow cylindrical structure of the CO bipolar outflow in the region. This work shows that the  $\text{H}_2\text{CO}$  6 cm line not only traces the outer envelope or quiescent states of molecular clouds but also gives information about the kinematics of the active regions of star formation.

E. A. gratefully acknowledges support from a NSF NRAO Student Support Fellowship (GSSP 05-0006). The authors also thank H. Hernández for the flexibility in the scheduling of the observations and NAIC for economic support to conduct the observations and to cover the page charges. We also acknowledge comments by an anonymous referee. P. H. acknowledges support from NSF grant AST 04-54665. H. L. was supported by a postdoctoral stipend from the German Max Planck Society. This research has made use of NASA's Astrophysics Data System.

## REFERENCES

- Araya, E., Baan, W., & Hofner, P. 2004a, *ApJS*, 154, 541  
 Araya, E., Hofner, P., Churchwell, E., & Kurtz, S. 2002, *ApJS*, 138, 63  
 Araya, E., Hofner, P., Goldsmith, P., Slysh, S., & Takano, S. 2003, *ApJ*, 596, 556  
 Araya, E., Hofner, P., Goss, W. M., Kurtz, S., Linz, H., & Olmi, L. 2006, *ApJ*, 643, L33  
 Araya, E., Hofner, P., Kurtz, S., Linz, H., Olmi, L., Sewilo, M., Watson, C., & Churchwell, E. 2005, *ApJ*, 618, 339  
 Araya, E., Hofner, P., Linz, H., Sewilo, M., Watson, C., Churchwell, E., Olmi, L., & Kurtz, S. 2004b, *ApJS*, 154, 579  
 Downes, D., Wilson, T. L., Bieging, J., & Wink, J. 1980, *A&AS*, 40, 379  
 Duncan, R. A., Forster, J. R., Gardner, F. F., & Whiteoak, J. B. 1987, *MNRAS*, 224, 721  
 Garrison, B. J., Lester, W. A., Miller, W. H., & Green, S. 1975, *ApJ*, 200, L175  
 Goodman, A. A., Benson, P. J., Fuller, G. A., & Myers, P. C. 1993, *ApJ*, 406, 528  
 Heiles, C. 1973, *ApJ*, 183, 441  
 Kenyon, S. J., Dobrzycka, D., & Hartmann, L. 1994, *AJ*, 108, 1872  
 Kutner, M., & Thaddeus, P. 1971, *ApJ*, 168, L67  
 Moriarty-Schieven, G. H., Snell, R. L., Strom, S. E., & Grasdalen, G. L. 1987, *ApJ*, 317, L95  
 Palmer, P., Zuckerman, B., Buhl, D., & Snyder, L. E. 1969, *ApJ*, 156, L147  
 Press, W. H., Teukolsky, S. A., Vetterling, W. T., & Flannery, B. P. 1999, *Numerical Recipes in C* (2nd ed.; Cambridge: Cambridge Univ. Press)  
 Rodríguez, L. F., Porras, A., Claussen, M. J., Curiel, S., Wilner, D. J., & Ho, P. T. P. 2003, *ApJ*, 586, L137  
 Rodríguez, L. F., et al. 1998, *Nature*, 395, 355  
 Sandqvist, A., & Bernes, C. 1980, *A&A*, 89, 187  
 Sewilo, M., Watson, C., Araya, E., Churchwell, E., Hofner, P., & Kurtz, S. 2004, *ApJS*, 154, 553  
 Takakuwa, S., et al. 2004, *ApJ*, 616, L15  
 Tucker, K. D., Tomasevich, G. R., & Thaddeus, P. 1970, *ApJ*, 161, L153  
 Uchida, Y., Kaifu, N., Shibata, K., Hayashi, S. S., Hasegawa, T., & Hamatake, H. 1987, *PASJ*, 39, 907  
 Watson, C., Araya, E., Sewilo, M., Churchwell, E., Hofner, P., & Kurtz, S. 2003, *ApJ*, 587, 714  
 Young, K. E., Lee, J. E., Evans, N. J., II, Goldsmith, P. F., & Doty, S. D. 2004, *ApJ*, 614, 252  
 Zuckerman, B., Palmer, P., & Rickard, L. J. 1975, *ApJ*, 197, 571